TRENDS IN SCIENCES 2026; 23(3): 12134
https://doi.org/10.48048/tis.2026.12134 RESEARCH ARTICLE

Controlled Thermal Oxidation of TiO_2-MXene: A Scalable Annealing Strategy for High-Performance Asymmetric Supercapatteries

Nida Usholihah[1,2], Ishmah Luthfiyah[3], Worawat Meevasana[3], Herlin Pujiarti[1,2], Apriharta[4], Malik Maaza[5], Muhamad Subhan Septian[1,2] and Markus Diantoro[1,2,*]

[1]Department of Physics, Faculty of Mathematics and Natural Science, Universitas Negeri Malang, Malang 65145, Indonesia
[2]Center of Advanced Materials for Renewable Energy, Universitas Negeri Malang, Malang 65145, Indonesia
[3]School of Physics, Faculty of Science, Suranaree University of Technology, Nakhon Ratchasima 30000, Thailand
[4]Department of Electrical Engineering and Informatics, Faculty of Engineering, Universitas Negeri Malang, Malang 65145, Indonesia
[5]Nanoscience and Nanotechnology, University of South Africa, Pretoria, South Africa

([*]Corresponding author's e-mail: markus.diantoro.fmipa@um.ac.id)

Received: 1 October 2025, Revised: 29 October 2025, Accepted: 2 November 2025, Published: 20 December 2025

Abstract

Enhancing the faradaic storage mechanism, stability, high power density, and energy density of energy storage requires further development of MXene, an oxidation-prone material, while preserving its interlayer structure and stability from restacking and excessive oxidation. This work presents a novel controlled thermal oxidation strategy, a scalable single-step annealing method to incorporate TiO_2 into MXene and engineer its surface chemistry without multi-step synthesis and other chemical additions. It has been successfully established that anatase TiO_2, structural defects, and oxide functional groups, which are critical for enhancing the redox reaction kinetics formed by the annealing treatment in the temperature range of 350 - 650 °C under air conditions. Among the annealed samples, TiO_2-modified MXene treated at 350 °C exhibited the most promising electrochemical performance. Its effective redox reactions demonstrated a battery-type behavior, dominated by diffusion-controlled charge storage, instead of the typical capacitive behavior driven by surface area. This was owing to an optimal balance between TiO_2 particle formation and the surface functional groups. Excessive oxidation at higher temperatures results in predominant TiO_2 formation, blocking interlayer spacing, and reducing the specific surface area. The specific capacitance (Cs) of MXene TiO_2 at 350 °C increases by up to 13% from the Cs of MXene reached 289.58 F/g at a scan rate of 20 mV/s, indicating superior electrochemical performance. Furthermore, an asymmetric supercapattery was manufactured by pairing MXene TiO_2 350°C with activated carbon (AC) as a practical approach to improving the energy density without sacrificing power density or capacity retention of the device. AC//MXene TiO_2 350 °C supercapattery demonstrates remarkable performance with a Cs of 49.42 F/g, energy density (ED) of 32.88 Wh/kg, and power density (PD) of 700.38 W/kg. Furthermore, it also demonstrated exceptional cycle stability (retaining 92% of its capacity after 5,000 cycles), and reduced resistance (equivalent series resistance (ESR), charge transfer resistance (Rct), and ion diffusion resistance), outperforming traditional AC-based supercapatteries. These findings highlight the novelty of controlled thermal oxidation as a simple yet effective route for engineering high-performance TiO_2-MXene-based electrodes for advanced energy storage systems.

Keywords: TiO_2 MXene, Controlled thermal oxidation, Annealing strategy, Asymmetric supercapattery, Faradaic performance, Energy density, Power density, Cycle stability, Scalable process

Introduction

The rising global requirement for advanced energy storage systems has become a major catalyst for research, focusing on the creation of devices that mitigate the performance trade-off between high-power supercapacitors and high-energy batteries [1]. Consequently, the escalating need for efficient clean energy storage in industrial applications has placed supercapacitors and batteries at the center of significant research and attention over the past decade [2]. The battery possesses a high energy density (~8 - 600 Wh/kg), but it is limited by poor cycling stability and low power density [3]. Meanwhile, a supercapacitor has high power density (10 kW/kg), long and stable cycle life, but poor energy density [4]. Hybrid asymmetric supercapacitors, or "supercapatteries," are an emerging class of hybrid devices that synergistically combine the distinct advantages of 2 electrode types: The high energy capacity of a battery and the high power delivery (rapid kinetics) of a capacitor [5]. The supercapacitor's EDLC electrode, which stores charge via ion adsorption at the electrolyte interface, acts as the power source. Conversely, the battery-type electrode, leveraging Faradaic redox characteristics, functions as the energy source [6]. The success of these devices hinges on the development of advanced electrode materials capable of sustaining both high power and high energy densities. In this context, 2-dimensional (2D) transition metal carbides and nitrides, known as MXenes, and specifically $Ti_3C_2T_x$, have garnered immense attention as a revolutionary material for electrochemical energy storage [7].

MXene, a 2-dimensional transition metal carbide, nitride, and carbonitride, is emerging as a promising electrode material for supercapacitors. Owing to its unique combination of metallic conductivity, a hydrophilic surface, and a layered structure analogous to graphene, $Ti_3C_2T_x$ MXene offers an excellent platform for rapid ion transport and charge storage [8]. MXene was first discovered by Gogotsi at Drexel University in 2011 [9]. MXene ($M_{n+1}X_nT_x$) can be obtained through selective etching, which removes the A layer from the MAX ($M_{n+1}AX_n$) phase. M refers to an early transition metal (Ti, Zr, Mo, etc.), A represents an element group of IIIA or IVA (Si, Ga, Al, etc), X is a carbon (C), and nitrogen (N), and T_x is surface terminal groups (-F, -O, or -OH) [8,10]. Among the discovered 30 MXene phases, $Ti_3C_2T_x$ has an advantage in ultra-high conductivity (~15.000 S/cm) [8]. Therefore, MXene can be a potential intrinsic electro-active material 2D material for high-performance supercapacitor electrodes [11].

First, the strong van der Waals forces between individual MXene nanosheets lead to inevitable restacking during electrode processing, which severely diminishes the electrochemically active surface area and obstructs electrolyte ion diffusion pathways. This restacking limits the redox reaction, thus leading to poor supercapacitor performance [12]. In addition, MXene has an intrinsic drawback, namely, poor oxidative stability, which leads to easy oxidation in ambient atmospheres [13]. Second, the charge storage mechanism in pristine MXene is predominantly based on electric double-layer capacitance (EDLC) and limited surface pseudocapacitance from its native functional groups (e.g., -OH, -O, -F). This capacitive behavior, while enabling high power, inherently limits the material's specific capacity and overall energy density, falling short of battery-level performance. This drawback was exploited to form a hybrid with TiO_2 using annealing treatment, acting as a spacer to enhance ion transportation and stabilize the MXene structure. The interaction between the Ti element of MXene ($Ti_3C_2T_x$) with the presence of oxygen in air leads to TiO_2 formation [14]. Because of its low cost, non-toxicity, chemical stability, and easy availability, TiO_2 has drawn interest in supercapacitor research [15]. However, the functional group of -F contribution to the redox storing mechanism is still unknown, and hardly provides a capacitive contribution [9,16]. Meanwhile, the oxygen and titanium vacancies will improve the storage capability, thus enhancing the performance of redox material [17]. Therefore, during the annealing treatment, exposed Ti due to the vacancy of -F functional group will be oxidized and replaced by –OH or =O [18].

TiO_2 can demonstrate enhanced redox activity and charge transport properties for a supercapacitor [17]. Kumar *et al.* [19] demonstrate that a supercapacitor-based MXene-TiO_2 has a higher capacity, up to 25%, compared to a pure MXene layer. MXene TiO_2 can be addressed using several methods, such as wet chemical

(hydrothermal), flashlight, and annealing treatment in the air. Compared to other methods, annealing treatment is a facile approach that does not require additional chemical processes, making it more environmentally friendly. It also offers a short and simple synthesis process and supports scalable production with consistent results. However, MXene TiO_2 by annealing treatment still exhibits poorer electrochemical performance compared to the wet chemical methods. Xie *et al.* [15] synthesized a fluorine-free MXene/TiO_2 composite by the hydrothermal method, resulting in a high specific capacitance (321 F/g) with excellent stability (81.7% after 10.000 cycles) [15]. Hong *et al* (2024) fabricate a porous MXene-TiO_2 anode with the help of a flashlight as a lithium-ion battery anode exhibiting improved Li^+ storage capacity (148 mAh/g) than pristine MXene with cycle stability up to 1,500 cycles [20]. Meanwhile, Sahu *et al.* [17] synthesized MXene-TiO_2 by annealing treatment for 1h at a temperature of 400 °C in the air, achieving a high specific capacitance of 186 F/g and excellent stability, showing 94% capacitance retention after 5,000 cycles. Furthermore, the modification of MXene TiO_2 by the annealing treatment in the air requires further investigation at various temperatures to determine the optimal conditions. When MXene is heated at low temperatures (150 - 350 °C), the intercalated H_2O and the other physically adsorbed molecules, such as -OH, -F, and -Cl, are removed, while the MXene structure remains intact [21]. At the higher temperatures, the defunctionalization and surface oxidation occur, leading to the formation of transition metal oxide, CO, and water terminations [22].

The previous studies have demonstrated that incorporating TiO_2 into MXene effectively enhances redox activity, hence improving the overall electrochemical energy storage performance. However, the most reported synthesis method relies on complex, multi-step wet-chemical methods (e.g., hydrothermal), which can be difficult to scale and often result in non-uniform material deposition and poor interfacial contact. Although one-step annealing treatment has been explored as a simpler alternative, it still faces challenges in preserving the MXene interlayer structure and stability caused by restacking and excessive oxidation. To address these limitations, there remains a critical need for a facile, scalable, and in situ strategy that can simultaneously engineer the MXene TiO_2 surface chemistry and morphology to unlock its full faradaic potential. This study presents a novel and highly scalable approach to overcome these challenges through a controlled thermal oxidation process. This research proposes a simple, one-step annealing treatment in an ambient air atmosphere as an elegant method to engineer the electrochemical properties of $Ti_3C_2T_x$ MXene. The novelty of this strategy lies in its dual functionality: (1) it facilitates the in-situ formation of anatase TiO_2 nanocrystals directly on the MXene surface, which serve as both redox-active sites and robust pillars to prevent nanosheet restacking; and (2) it simultaneously modifies the surface chemistry by removing inert functional groups (e.g., -F) and introducing more electrochemically active Ti-O bonds. Hypothesize that by precisely tuning the annealing temperature, we can achieve an optimal balance between creating these beneficial features and preserving the conductive Ti_3C_2 core, thereby fundamentally shifting the charge storage mechanism from capacitive to diffusion-controlled, battery-type behavior. To validate this approach, we systematically investigate the effect of annealing temperature (350, 450, 550, and 650 °C) on the structural, chemical, and electrochemical properties of $Ti_3C_2T_x$. We demonstrate that the optimized material, annealed at 350 °C, delivers a remarkable specific capacitance and exhibits clear battery-type characteristics. Furthermore, we validate its practical utility by fabricating a high-performance asymmetric supercapattery device, pairing the modified MXene with an activated carbon electrode. This work establishes controlled thermal oxidation as a powerful and commercially viable route for engineering next-generation MXene-based electrodes for advanced energy storage systems.

Materials and methods

Materials

The materials used in this study include MAX phase Ti_3AlC_2 (Luoyang Tongrun Info Technology CO., LTD., specific 98 wt% pure, 200 mesh), hydrofluoric acid (HF) (Sigma-Aldrich, 48% purity), DI water (OneMed, 99%), alcohol (OneMed, 96%), aquadest (Brataco), dimethylacetamide (DMAC, Merck, Darmstadt, Germany), ET_4NBF_4 (Gelon, Shandong, China), acetonitrile (Merck, Darmstadt, Germany), Cu foil, polyvinylidene fluoride (PVDF) (Sigma-Aldrich,

Burlington, MA, USA), carbon black (CB) (Imerys, La Hulpe, Belgium), cellulose separator, commercial activated carbon (AC) (CGC, Bangkok, Thailand), and coin cell sets (TOB Machine, Fujian, China).

Synthesis and modification of MXene

The Al layer from Ti_3AlC_2 was removed using a selective etching process using an HF solution. The 1 g MAX powder was completely dissolved in 20 mL of HF and then mixed for 24 h. The sediments were washed with DI water until the supernatant pH was higher than 6. The sediment was dried using a hot plate at 100 °C for 6 h, resulting in MXene powders. The MXene TiO_2 was achieved by annealing the MXene powder at various temperatures (350, 450, 550, and 650 °C) using a furnace under air conditions for 1 h. MXene synthesis and modification illustrations are shown in **Figure 1(a)**.

Fabrication coin cells

The MXene slurry was mixed in a DMAC solution in an 8:1:1 ratio of MXene as the active material, PVDF as the binder, and CB as the conductive agent, respectively. First, PVDF was dissolved in DMAC at 80 °C until it was completely homogenized. After that, CB and MXene are slowly mixed into the slurry, then stirred for 6 h. The slurry was stirred for 6 h at room temperature until the solution was completely homogeneous. Next, the slurry was deposited using a doctor blade on Cu foil with a thickness of 20 µm. The deposited samples were then dried in an oven at 100 °C for 24 h. The electrodes were manufactured into coin cells with 1 M ET_4NBF_4 as the electrolyte and cellulose as a separator, as shown in **Figure 1(b)**.

Characterization

The morphological characteristics and composition of the samples were characterized using Scanning Electron Microscopy (SEM-EDX, SEM-EDX FEI Type INSPECT-S50). The crystal phase of the samples was characterized using X-Ray Diffraction (XRD, PAN Analytical type EXPERT-3). The chemical bonds formed were determined using Fourier Transform Infrared (FTIR, Shimadzu type IR Prestige 21). The sample's surface area and porosity were characterized using Brunauer-Emmett-Teller (BET SA, Bellsorp mini X). Then, the electrochemical measurements of coin cells were carried out using Cyclic Voltammetry (CV), Electrochemical Impedance Spectroscopy (EIS), and Galvanostatic Charge Discharge (GCD) by Cortest and Neware 3000. The MXene electrodes' performance was characterized with CV using a 3-electrode system, including the MXene electrode as a working electrode, Ag/AgCl as a reference, and Pt as a counter electrode. Meanwhile, the supercapattery device was characterized using a 2-electrode system in the form of a coin cell device, characterized with CV, EIS, and GCD.

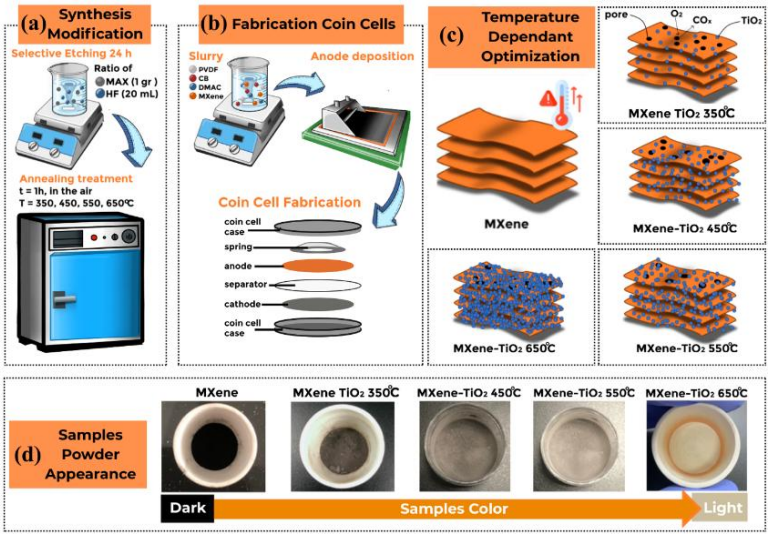

Figure 1 Schematic illustration of the (a) MXene synthesis by HF etching and subsequent annealing in air at varying temperatures (350 - 650 °C), (b) Fabrication process of the coin cell supercapattery, including slurry preparation, electrode deposition, and cell assembly with activated carbon as the cathode and MXene or MXene-TiO_2 composites as the anode, (c) the temperature-dependent optimization of MXene, and (d) Final appearance of sample powder.

Electrochemical measurements

The performance of the supercapattery was analyzed after calculating several parameters, including specific capacitance, energy density, and power density. Capacitance is the ability of a material to hold an electrical charge [23]. Meanwhile, specific capacitance can be defined as capacitance related to a specific entity, such as area, volume, or mass [24]. In this research, gravimetric capacitance has been calculated based on the mass of the electrode's active material, expressed in Farads per gram (F/g) [25]. CV test was carried out in a 3-electrode system for a single electrode (C_g) and a 2-electrode system for a coin cell device(C_{cell}). CV curves can be used to calculate the specific capacitance of a single electrode (${C_g}^{CV}$) and the 2-electrode cell (${C_{cell}}^{CV}$) using Eq. (1) [26].

$$ {C_g}^{CV} = 4 \times {C_{cell}}^{CV} = 4\frac{\int I\, dV}{2 \times m \times v \times \Delta V} \quad (1) $$

where $\int_{vc}^{va} I\, dV$ is the CV curves area (W), v is the scan rate, and m is the mass of the electrode active material, and ΔV is the potential window.

The specific capacitance, energy density, and power density of the supercapattery device were obtained through GCD using Eqs. (2) - (4), respectively [27].

$$ {C_g}^{CD} = 4 \times {C_{cell}}^{CD} = 4\frac{\Delta t \times I}{m \times \Delta V} \quad (2) $$

$$ ED = \frac{{C_{cell}}^{CD} \times \Delta V^2}{2 \times 3.6} \quad (3) $$

$$ PD = \frac{3600 \times ED}{\Delta t} \quad (4) $$

where Δt are discharging time (s), I is current, ED represents the energy density (Wh/kg), and PD is power density (W/kg).

To confirm the storage mechanism of materials, the relationship between peak current and scan rates according to Power's law is used, shown in Eq. (5), where i, a, and v^b represent the peak current, scan rate, and constants, respectively. The b value can be determined from the slope of log (v) vs log (i) plot from Eqs. (6) - (7). According to the Randles-Sevcik equation, b = 0.5 indicates that the electrochemical storage mechanism is dominated by diffusion control for battery-like materials. Meanwhile, the value b = 1 indicates the dominance of the capacitive-controlled for EDLC and pseudocapacitive materials [6,28]. For further analysis of the capacitive and diffusive contributions, the power law equation can be modified into Eq. (8). If the relationship between i and v is linear ($i \propto v^1$), the charge storage reaction is limited by the capacitive control. While if the relationship between i and v is nonlinear ($i \propto v^{1/2}$), the charge storage reaction is limited by diffusion [28]. The constants k_1 and k_2 represent the contribution of capacitive-controlled and diffusive-controlled, and can be evaluated by the slope and the intercept of $v^{\frac{1}{2}}$ vs $i(V)/v^{\frac{1}{2}}$ [29].

$$ i = av^b \quad (5) $$

$$ \log i = b\, logv + \log a \quad (6) $$

$$ b = \frac{logi}{logv} - logv\ a \quad (7) $$

$$ i(V) = k_1 v + k_2 v^{\frac{1}{2}} \quad (8) $$

Results and discussion

The key findings of this research are the successful utilization of **controlled thermal oxidation** as a scalable strategy to transform MXene ($Ti_3C_2T_x$) into an MXene-TiO_2 composite. The annealing temperature serves as a key parameter controlling the material's final properties, as demonstrated by various characterization techniques. By visual observation, the appearance of the thermally treated MXene powder serves as preliminary evidence of TiO_2 production, shown in **Figure 1(d)**. As the temperature rises, MXene gradually loses color from its original black into a greyish tone, and finally to opaque (MXene TiO_2 650 °C**)**. This steadily fading demonstrated the rising formation of TiO_2, which normally has an opaque white color [30].

Controlled thermal oxidation: Driving phase transformation and crystallinity in MXene TiO_2

To clarify the transformation due to thermal oxidation, **X-Ray Diffraction (XRD)** analysis was used

to observe the phase evolution and crystallinity from MAX phase to MXene and subsequently to the MXene TiO_2. The XRD spectra in **Figure 2(a)** chart the structural evolution from the MAX phase to MXene and finally to MXene-TiO_2 composites. The complete disappearance of Al peaks confirms the successful etching of the MAX phase (Ti_3AlC_2) to produce MXene ($Ti_3C_2T_x$), characterized by its distinct (003), (004), (011), (013), (008), and (111) peaks [20]. After annealing, a significant structural transformation occurs. The original MXene peak decreases, leaving peaks at orientations such as (008), (013), and (111), indicating disruption of the layered nanosheet structure of MXene due to oxidation [31]. The d-spacing of MXene before and after annealing was 1.90 and 1.89 Å, respectively, indicating that the **annealing process has a negligible effect on the interlayer spacing**. Crucially, new peaks appear corresponding to the anatase phase of TiO_2 - specifically (101), (103), (004), (105), (211), (116), (220), (301), and (224) [19]. The dominance of the anatase phase, known to form under rapid oxidation conditions, confirms that our annealing strategy successfully induces a fast conversion of the MXene surface to TiO_2 [32]. This transformation is a direct result of the controlled thermal oxidation, where the growth of TiO_2 peaks occurs at the expense of the original MXene signatures. This signifies a clean phase evolution where the original MXene structure is consumed to form TiO_2 crystals.

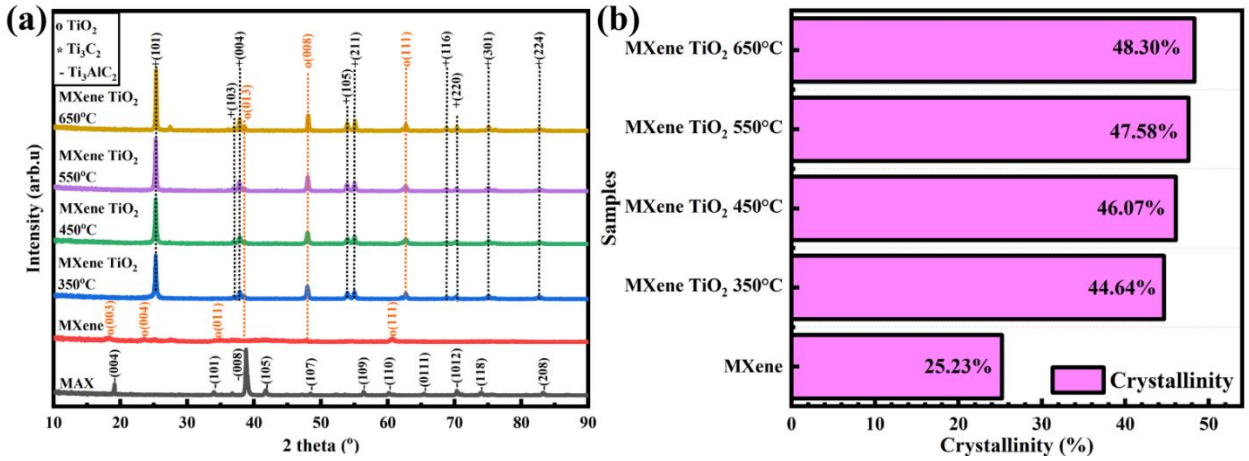

Figure 2 The histograms of (a) X-ray Diffraction (XRD), (b) Crystallinity as a function of annealing temperature.

Figure 2(b) shown derived from the XRD data, quantitatively shows the MXene lattice's crystallinity as a function of annealing temperature. Crucially, increasing the annealing temperature resulted in a direct, positive correlation with the material's overall crystallinity (from 44.69% at 350 °C to 48.30% at 650 °C), substantially higher than that of pure MXene (25.23%). This observation confirms that despite the inherent structural weakening caused by rapid oxidation, the highly crystalline anatase TiO_2 phase successfully dominates the composite structure, dictating the enhancement in crystallinity. Theoretically, the strong oxidation rate weakens the crystal structure of the material, thus also reducing the crystallinity [15]. This result confirms that the controlled thermal treatment promotes the formation of a highly crystalline anatase TiO_2 phase, which acts as the dominant crystalline structure, thus enhancing the overall crystallinity of the composite.

Chemical and elemental evolution: Confirming the oxidation mechanism

The profound phase and structural changes confirmed by XRD and crystallinity data are further quantified and validated by Energy-Dispersive X-ray Spectroscopy (EDX) and Fourier Transform Infrared (FTIR) analysis.

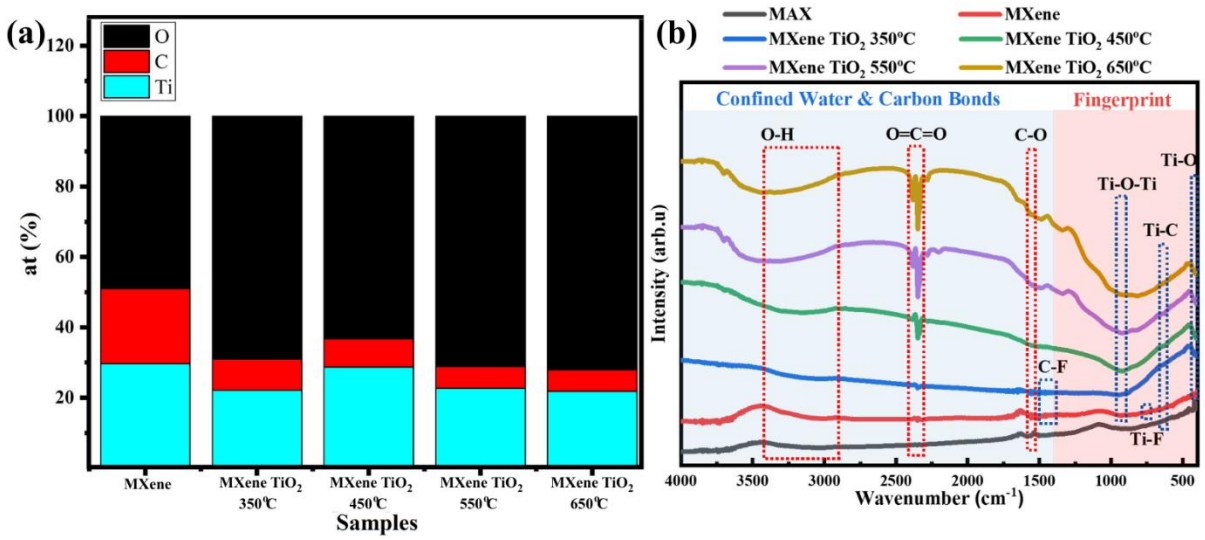

Figure 3 (a) Elemental composition by Energy-Dispersive X-ray Spectroscopy (EDX), and (b) functional bonds spectra by Fourier-Transform Infrared Spectroscopy (FTIR) of the samples

Figure 3(a) shows the EDX data provide elemental evidence of the oxidation process: as the annealing temperature increased, the atomic ratio shown in **Table 1**. Carbon (C) decreased gradually (from 21.41% to 6.10%), while the ratio of Oxygen (O) increased substantially (from 48.95% to 72.01%). This inverse elemental relationship directly confirms the chemical mechanism where exposed MXene interacts with ambient oxygen. C atoms are consumed by forming CO_x gases, leading to the observed loss of C content, thus generating pore formation. While Ti atoms readily bond with the increasing amount of O, resulting in TiO_2 . The schematic process can be illustrated as in **Figure 1(c)**. TiO_2 formation was definitively detected in the EDX data beginning at 350 °C, consistent with the initial appearance of anatase peaks in the XRD pattern at this same temperature.

Figure 3(b) shows the FTIR spectra, revealing the evolution of chemical functional groups across the samples. FTIR analysis provides further evidence of the chemical changes induced by HF etching and thermal oxidation. First, the FTIR region corresponding to the fingerprint vibration of the material in the range of 400 - 1,400 cm^{-1} [33]. Materials fingerprint vibration, including Ti-O stretching [34], Ti-C stretching, Ti-F bending [33], Ti-O-Ti [35], and C-F stretching [33], are detected at wavenumbers of 400 - 430, 631, 756, 923 and 1,300 - 1,500 cm^{-1}, respectively. Second, the FTIR region corresponding to confined water and carbon bond vibrations, in the range of 1,400 - 4,000 cm^{-1}. Confined water vibrations, including O-H *stretching* [36], were detected at wavenumbers of 2,900 - 3,500 cm^{-1}. The carbon bond vibration, including C-O stretching [37], and O=C=O bonds [38] were detected at wavenumbers of 1,557 and 2,300 - 2,400 cm^{-1}. The spectrum of MXene, compared to the MAX phase, shows the appearance of new vibrations - including C-F stretching, Ti-F bending, Ti-O stretching, and Ti-O-Ti-confirming that HF etching successfully replaced Al atoms with oxygen- and fluorine-containing functional groups (-O, -OH, -F) [7]. The FTIR spectra of the annealed samples reveal the progression of oxidation. The Ti-F bond disappears entirely after heat treatment, and the C-F bond weakens significantly in MXene TiO_2 350°C and vanishes at higher temperatures. Concurrently, the intensities of the Ti-O and Ti-O-Ti peaks deepen with increasing temperature, confirming the increasing formation of more TiO_2 [20]. The appearance and intensification of C-O stretching and O=C=O bonds indicate carbon oxidation and CO_2 adsorption on the material surface during annealing [34,39]. The persistence of the Ti-C bond across all samples except MXene TiO_2 650 °C suggests the core MXene structure remains largely intact up to 550 °C, with severe oxidation occurring only at the highest temperature.

The chemical and morphological evolution resulting from this controlled oxidation process profoundly influences the material's suitability for electrochemical applications. FTIR spectroscopy provided molecular evidence of the oxidation, showing

the complete removal of unstable surface fluorides (Ti-F and C-F), concurrent with the deepening of Ti-O and Ti-O-Ti bonds, confirming the increased formation and structural integration of TiO_2. The FTIR spectroscopy provided a molecular link to this elemental shift: the progressive deepening of the Ti-O and Ti-O-Ti bond peaks confirmed the structural establishment of TiO_2, while the appearance of C-O and O=C=O bonds corroborated the EDX finding that C oxidation occurred during heat treatment. The loss of C atoms and the simultaneous generation of CO_x gas are also the fundamental drivers for pore formation observed in the SEM and N_2 adsorption analysis, reinforcing the interconnected nature of the controlled thermal process.

Table 1 The atomic composition (%) of the samples by EDX.

Elements	MXene	MXene TiO_2 350 °C	MXene TiO_2 450 °C	MXene TiO_2 550 °C	MXene TiO_2 650 °C
Ti	29.65	22.14	28.78	22.76	21.89
C	21.41	8.86	8.00	6.14	6.10
O	48.95	69.00	63.22	71.10	72.01

Textural Properties and the Oxidation Trade-Off (Porosity and SSA)

Figures 4(a) and **4(b)** Adsorption-Desorption Isotherms and Pore Size Distribution. The textural properties, which are critical for ion transport in supercapatteries, reveal a crucial trade-off driven by the oxidation level. N_2 adsorption-desorption isotherms are shown in the graph from **Figure 4(a)**. All samples demonstrate a type IV isotherm and H3 hysteresis loop. The isotherm IV type is related to mesoporous materials (2 - 50 nm in diameter) [40]. The H3 loop type suggests the presence of plate-like particles forming non-rigid aggregates, typical of the MXene-derived structure. The loss of C atoms and the generation of CO_x gas during oxidation directly led to the formation of these pores; consequently, pore size generally increased with annealing temperature due to the accelerating oxidation rate (as confirmed by EDX. The pore diameter and specific surface area of the samples are shown in **Table 2**. All the materials have diameters in the range of 4 - 49 nm, indicating mesoporous materials, as confirmed by the Barret-Joyner-Halenda (BJH) pore size distributions in **Figure 4(b)**. From these results, it can be confirmed that the higher the annealing temperature, the higher the oxidation level, and thus the pore size formed is larger, except for MXene at 650°C. However, despite the larger pore size, the Specific Surface Area (SSA) exhibited a drastic decrease as the temperature rose (from 35.6 m^2g^{-1} for pure MXene down to a minimum of 10.3 m^2g^{-1} at 550 °C). This reduction is the direct consequence of the high TiO_2 formation (validated by XRD and high O content in EDX) at elevated temperatures. Specifically, the large amount of TiO_2 acts detrimentally by covering the exposed MXene pores and filling the critical interlayer spacing. This TiO_2 blockage prevents the surface area from increasing and, critically, inhibits ion transportation rather than acting as a beneficial spacer to prevent self-restacking. MXene 650 °C has the highest number of TiO_2 confirmed by EDX and XRD. The specific surface area of pure MXene, MXene 350 °C, MXene 450 °C, MXene 550 °C, and MXene 650 °C are 35.6, 25.6, 14.5, 10.3, and 15.7 m^2g^{-1}, respectively. The surface area value decreases with increasing annealing temperature, despite the pore size increasing. This is because the surface area is also affected by other factors, such as the number and size of MXene pores, the value of MXene interlayer spacing, and the amount and size of TiO_2 [19,41]. Based on the XRD data, the annealing treatment (from 350 to 650 °C) has a negligible effect on the interlayer spacing; therefore, the decrease in surface area is mainly attributed to the formation of TiO_2. The surface area will not increase when TiO_2 covers the pores and the MXene interlayer spacing, despite the increase in the number of pores. Additionally, a TiO_2 size that is too large will occupy the interlayer space, preventing it from acting as a spacer and inhibiting ion transportation.

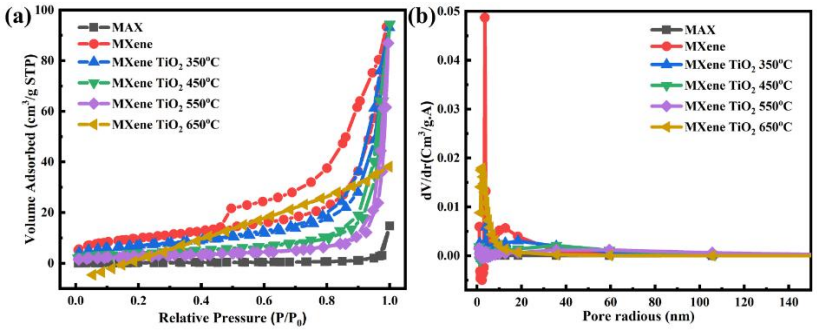

Figure 4 (a) N_2 adsorption-desorption isotherms of the samples, and (f) BJH pore size distribution of MXene samples.

Table 2 The pore diameter of pure MXene and modified MXene samples.

Samples	MAX	MXene	MXene TiO_2 350 °C	MXene TiO_2 450 °C	MXene TiO_2 550 °C	MXene TiO_2 650 °C
Specific surface area (m^2g^{-1})	1.52	35.64	25.60	14.48	10.35	15.67
Total pore volume (cm^3g^{-1})	0.014	0.14	0.13	0.12	0.11	0.058
Pore diameter (nm)	18.03	8.05	10.20	16.83	20.32	7.40

Morphological evolution of MXene ($Ti_3C_2T_x$) during controlled thermal

The precursor MAX phase (Ti_3AlC_2) initially exhibits its characteristic bulk structure (**Figure 5(a)**). Following the Hydrofluoric acid (HF) etching process, the selective removal of the Al layer - a reaction that produces easily dissolved AlF_3 and H_2 gas - leads to the formation of the MXene $Ti_3C_2T_x$ structure [42,43]. This is distinctly observed as an accordion-like structure composed of multilayered nanosheets (**Figure 5(b)**). The subsequent controlled thermal oxidation induces significant morphological changes, primarily manifested as surface defects and pore formation, which directly affect ion transport kinetics.

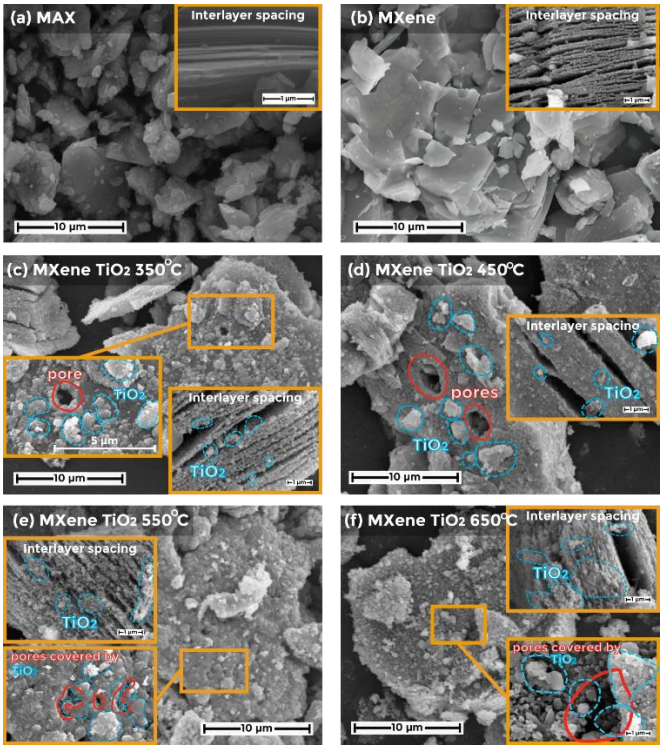

Figure 5 SEM-EDX images of (a) MAX, (b) pure MXene, (c) MXene TiO_2 350 °C, (d) MXene TiO_2 450 °C, (e) MXene TiO_2 550 °C and (f) MXene TiO_2 650 °C.

The heat treatment process induces morphological defects and pore formation on the surface of MXene. Clear evidence of pore formation is observed on MXene TiO_2 350 °C and MXene TiO_2 450 °C, with sizes of 0.8 µm (**Figure 5(c)**), 2.4 and 3.0 µm (**Figure 5(d)**). However, pore formation is not obvious in MXene TiO_2 550 °C and MXene TiO_2 650 °C, as a significant amount of TiO_2 completely covers the MXene flakes, as seen in **Figures 5(e) - 5(f)**. When the temperature increases to 550 and 650 °C, too many defects will form. Hence, oxidation will happen faster in the big defect than in the smaller defect, which can lead to the rapid formation of TiO_2 particles [32]. TiO_2 Overgrowth and Surface Blocking: However, at higher annealing temperatures (550 and 650 °C), the morphology shifts dramatically. The rapid increase in temperature creates numerous defects, which accelerate the oxidation rate. This leads to the rapid formation and overgrowth of TiO_2 particles at these defect sites. As seen in **Figures 5(e) - 5(f)**, a significant amount of TiO_2 now completely covers the MXene flakes. The oxidation process, which occurs at increasing annealing temperatures, plays a crucial role in forming pores and TiO_2 particles. This phenomenon is related to MXene's intrinsic property, which causes it to oxidize and degrade easily in ambient atmospheric conditions [13]. In the oxidation process, oxygen reacts and separates the carbon atoms from MXene $Ti_3C_2T_x$. CO_x gases will be created so that pores are successfully formed [44]. Moreover, oxygen will also easily bond with the Ti element from $Ti_3C_2T_x$ to create TiO_2 during the heat treatment [45].

Electrochemical Performance of MXene-TiO_2 anodes and asymmetric supercapatteries

This discussion analyzes the electrochemical performance of thermally oxidized MXene-TiO_2 electrodes, linking the findings directly to the research purpose of developing a scalable annealing strategy for high-performance asymmetric supercapatteries.

Three-electrode electrochemical analysis of MXene-TiO_2 Anodes

To discover the sample's performance and storage mechanism, all samples were tested in a 3-electrode system with Ag/AgCl reference at the various scan rates of 20, 30, 40, 50, 60, 80, and 100 mV/s.

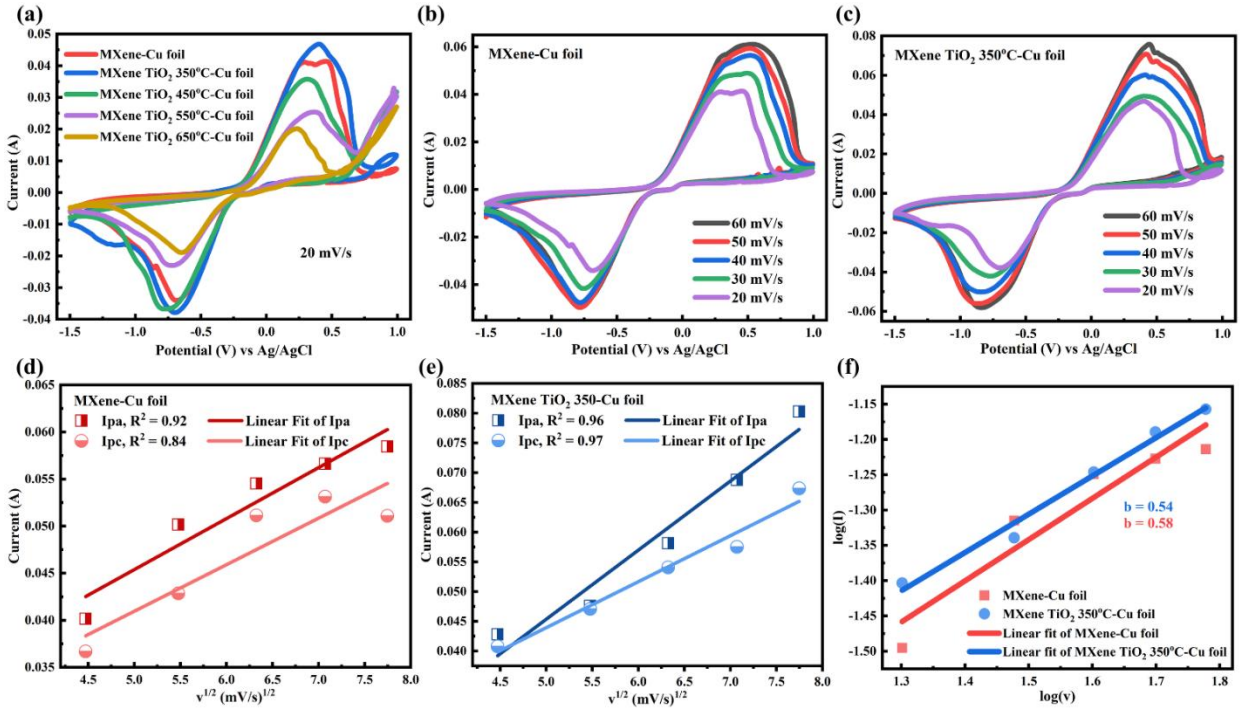

Figure 6 (a) CV curves of all samples at the scan rate of 20 mV/s, (b) CV curves of MXene-Cu foil at the various scan rates, (c) CV curves of MXene TiO_2 350 °C-Cu foil at the various scan rates, (d) Plot of the square root of scan rate vs the peak current of MXene-Cu foil, (e) Plot of the square root of scan rate vs the peak current of MXene TiO_2 350 °C-Cu foil, (f) Plot of log(v) vs log (I).

All sample' CV profiles show the non-rectangular and faradaic shape as a feature of the battery-like material [46], shown in **Figures 6(a)**. The occurrence of the faradaic redox reaction is indicated by the appearance of the redox peaks, including anodic (pa) and cathodic peaks (pc). MXene TiO_2 350 °C electrode demonstrated the highest specific capacitance (289.58 F/g at 20 mV/s), surpassing pristine MXene (228.03 F/g) and significantly outperforming materials annealed at higher temperatures, such as MXene TiO_2 650 °C (104.71 F/g). The complete capacitance values at 20 mV/s follow the sequence: MXene TiO_2 350 °C (289.58 F/g) > MXene TiO_2 450 °C (254.98 F/g) > pristine MXene (228.03 F/g) > MXene TiO_2 550 °C (147.32 F/g) > MXene TiO_2 650 °C (104.71 F/g). The specific capacitance at the other scan rates also demonstrates that MXene TiO_2 350 °C has the highest performance, shown in **Table 3**. This optimal result at MXene TiO_2 350 °C is a direct consequence of balancing TiO_2 anatase formation (confirmed by XRD and EDX) to introduce redox activity, with the preservation of sufficient specific surface area (SSA). Higher temperatures cause excessive TiO_2 growth, leading to particle blocking and catastrophic SSA reduction, thus hindering performance. The overall enhanced performance is attributed to the increase in redox reaction due to the diffusion of ions into the newly formed TiO_2 crystalline anatase phase, improved hydrophilicity, and the creation of electrochemically active defect sites on the MXene TiO_2 350 °C surface [17].

The mechanism that occurs inside the MXene-Cu foil and the MXene TiO_2 350 °C-Cu foil can be analyzed using CV curves at scan rates of 20, 30, 40, 50, and 60 mV/s (**Figures 6(b)** and **6(c)**). As the scan rates applied increase, the anodic and cathodic peaks are shifted into the higher and lower potential values, respectively, with the most obvious shift occurring in the MXene sample. This phenomena indicate the incomplete intercalation and deintercalation process of the electrolyte ion into the electrode material [29]. The fundamental charge storage mechanism was investigated by analyzing the kinetics of the electrochemical reaction. A linear relationship between the peak current and the square root of the scan rate (**Figures 6(d)** and **6(e)**) for both anodic and cathodic peaks, evidenced by R^2 values approaching 0.99, signifies an electrochemical process predominantly governed by semi-infinite diffusion. This behavior is characteristic of battery-type materials, where Faradaic charge transfer is limited by the solid-state diffusion of ions within the bulk electrode [47]. Further quantitative analysis of the charge storage kinetics was performed using the power-law relationship ($i = av^b$). The calculated *b*-values for MXene and MXene TiO_2 350 were 0.58 and 0.54, respectively (**Figure 6(f)**). These values, being closer to the theoretical limit of 0.5 for a diffusion-controlled process than to 1.0 for a surface-controlled capacitive process, confirm that the storage mechanism is primarily battery-type. Generally, from the previous studies, TiO_2 is suitable as a battery anode due to its redox kinetics [28]. The marginally higher b-value for pristine MXene implies a more non-negligible capacitive contribution, attributable to its larger specific surface area and wider interlayer spacing that facilitate electric double-layer formation and surface-mediated ion storage. The current response was deconvoluted into capacitive (k_1) and diffusion-controlled (k_2) contributions to provide a definitive quantification. The k_2 values (~7.19×10^{-3} for MXene and ~8.03×10^{-3} for MXene TiO_2 350 °C) were found to be an order of magnitude greater than the corresponding k_1 values (~10^{-4}), unambiguously verifying the dominance of the diffusion-controlled pathway.

Table 3 Specific capacitance of all samples deposited on Cu foil substrate at the various scan rates from the CV curves.

Scan Rate (mV/s)	Specific Capacitance (F/g)				
	MXene	**MXene TiO_2 350 °C**	**MXene TiO_2 450 °C**	**MXene TiO_2 550 °C**	**MXene TiO_2 650 °C**
20	254.98	289.58	228.03	147.32	104.71
30	210.91	230.49	201.56	120.90	79.44
40	195.20	214.30	148.63	108.90	63.75
50	175.33	193.37	134.82	102.66	50.35
60	143.17	170.65	121.97	106.67	43.45

Scan Rate (mV/s)	Specific Capacitance (F/g)				
	MXene	MXene TiO_2 350 °C	MXene TiO_2 450 °C	MXene TiO_2 550 °C	MXene TiO_2 650 °C
80	118.45	148.96	102.28	94.09	37.99
100	97.75	128.18	85.79	78.86	32.35

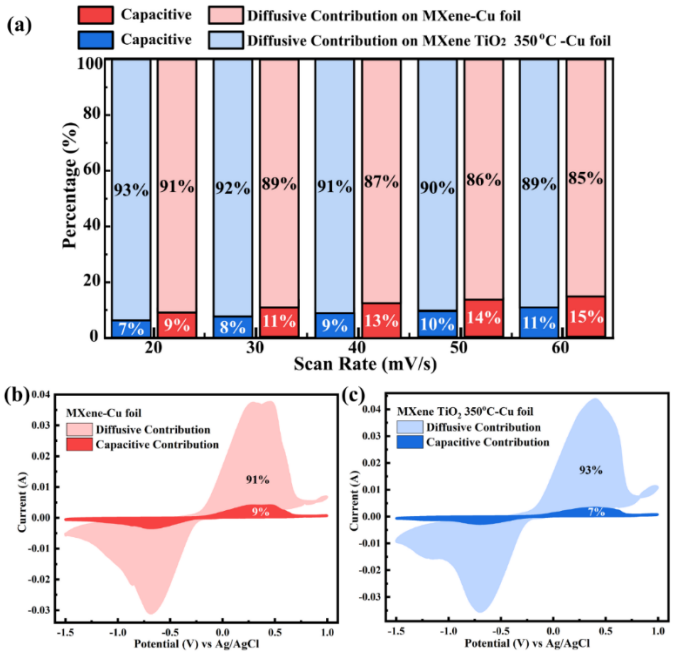

Figures 7 (a) Capacitive and diffusive contribution, and (b-c) CV curve with capacitive and diffusive distribution at the scan rate of 20 mV/s of MXene-Cu foil and MXene TiO_2 350 °C Cu foil.

Table 4 Electrode-based MXene performance comparison with existing research.

Sample	Synthesis	Electrolyte	Potential window (V)	Specific Capacitance (F/g)	Ref
$Ti_3C_2T_x$ TiO -np (nanoparticles)	Room temperature oxidation in H_2O solution	6M KOH	−1 to −0.4 V (vs Ag/AgCl)	128 F/g at 2 mV/s	[45]
$Ti_3C_2T_x$ TiO -nw (nanowires)	Room temperature oxidation in NaOH solution	6M KOH	−1 to −0.4 V (vs Ag/AgCl)	143 F/g at 2 mV/s	[45]
$Ti_3C_2T_x$ TiO_2 NG (nanogrooves)	Hydrothermal	6M KOH	0 to 1 V	81 F/g at 100 mV/s	[19]
$Ti_3C_2T_x$ TiO_2 (nanoparticles)	Annealing in air at 500 K (227 °C)	30 wt% KOH	0 to 0.7 V	~5 F/g at 5 mV/s	[48]
$Ti_3C_2T_x$ derived TiO_2 /C	Microwave irradiation in the air	-	−1 to −0.3 V (vs Hg/HgO)	28 F/g at 100 mV/s	[49]
$Ti_3C_2T_x$ TiO_2 (nanoparticles)	Annealing in air at 350 °C	1M Et_4NBF_4	−1.5 to 1 V (vs Ag/AgCl)	289.58 F/g at 20 mV/s	This work
$Ti_3C_2T_x$ TiO_2 (nanoparticles)	Annealing in air at 450 °C	1M Et_4NBF_4	−1.5 to 1 V (vs Ag/AgCl)	228.03 F/g at 20 mV/s	This work

The percentage of capacitive and diffusive contributions as a function of the scan rates can be shown in **Figure 7(a)**. Both samples show that the diffusion-controlled process was more dominant than the capacitive-controlled process. At the highest scan rate of 60 mV/s, MXene and MXene TiO_2 350 °C show that 85% and 89% of their capacitance was driven by the diffusion-controlled process. As the scan rates increase, the diffusion-controlled process contribution also increases. At the slow scan rate of 20 mV/s, MXene and MXene TiO_2 350 °C show that 91% and 93% of their capacitance was driven by the diffusion-controlled process, shown in **Figures 7(b)** and **7(c)**. The increase of diffusion-controlled contribution is caused by the rise of redox reaction due to TiO_2 addition in MXene TiO_2 350 °C [17]. This enhancement is directly correlated with the material's evolution; the controlled thermal oxidation at 350 °C generates electroactive anatase TiO_2 phases, which provide a high density of accessible sites for reversible redox reactions, thereby amplifying the diffusion-limited, Faradaic charge storage component. The optimized MXene TiO_2 350 °C sample demonstrates competitive electrochemical performance when benchmarked against composites synthesized via alternative methods, as cataloged in **Table 4**. This comparative analysis substantiates that controlled annealing at 350 °C constitutes a scalable and efficacious strategy for fabricating high-performance MXene-derived TiO_2 composites, positioning it as a viable and superior synthesis route for advanced energy storage materials. However, the electrode performances tend to deteriorate at the higher annealing temperatures (450, 550 and 650 °C). This is because the electrode-electrolyte contact area is reduced by too large a TiO_2 formation [8]. The excessive TiO_2 production will hinder the continuous electron transfer in the electrode, thus increasing the electrode resistance and lowering the electrochemical performance [20].

Performance of asymmetric supercapattery devices

The electrochemical performance of a supercapattery device based on MXene and MXene TiO_2 350 °C as an anode paired with an AC commercial cathode, was investigated using Cyclic Voltammetry (CV), Galvanostatic Charge Discharge (GCD), and Electrochemical Impedance Spectroscopy (EIS) in a 2-electrodel system configuration.

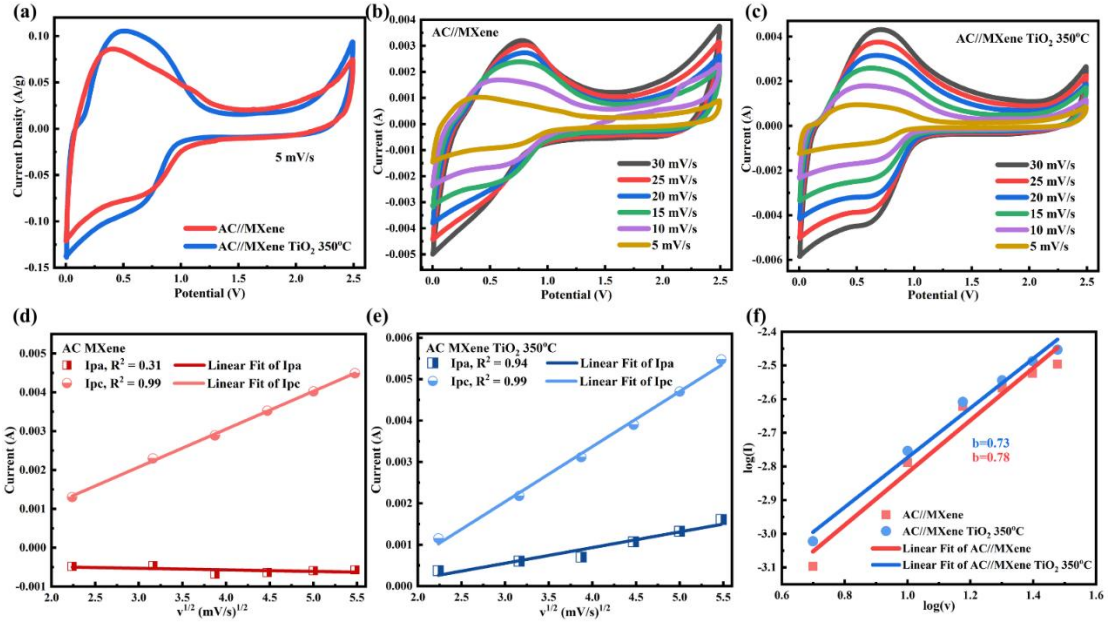

Figure 8 (a) CV curves of supercapattery based AC//MXene and AC//MXene TiO_2 350 °C at the scan rate of 5 mV/s, (b) CV curves of AC//MXene at the various scan rates, (c) Plot of the square root of scan rate vs the peak current of AC//MXene, (d) CV curves of AC//MXene TiO_2 350 °C at the various scan rates, (e) Plot of the square root of scan rate vs the peak current of AC//MXene TiO_2 350 °C, (f) Plot of log(v) vs log (I).

The CV curves were established at the scan rates of 5, 10, 15, 20, 25, 30, 40, 60, 80, and 100 mV/s. The CV curves show energy storage mechanism from the combination of an EDLC by AC material and a battery-type by MXene material (**Figure 8(a)**). The specific capacitance from the supercapattery device can be calculated using Eq. (1), shown in **Table 5**. Compared to AC//MXene, AC//MXene TiO_2 350 °C represents the highest specific capacitance in all scan rates. The highest capacitance was achieved by AC//MXene TiO_2 350 °C at a scan rate of 5 mV/s (50.50 F/g), surpassing that of AC//MXene (49.02 F/g). This result is compatible with the result of the CV 3-electrode system as described before. To confirm the mechanism inside the supercapattery devices, the CV curves at the scan rates of 5, 10, 15, 20, 25, and 30 mV/s can be used (**Figures 8(b)** and **8(c)**). The alignment of redox peaks serves as an indicator of the reversibility mechanism. The semi-reversible mechanism has the rapid peaks, and the irreversible mechanism shows the divergent peaks [46].

Table 5 Specific capacitance of AC//MXene and AC//MXene TiO_2 350 °C at the various scan rates from CV curves.

Samples	Specific Capacitance (F/g) at the Various Scan Rates (mV/s)									
	100	**80**	**60**	**40**	**30**	**25**	**20**	**15**	**10**	**5**
AC//MXene	15.64	16.93	21.73	24.08	25.43	28.37	31.25	38.43	38.60	49.02
AC//MXene TiO_2 350 °C	26.91	27.62	32.14	38.60	42.07	44.27	46.42	48.53	50.17	50.50

The R^2 values close to 1 indicate the linear relationship, thus showing the good reversibility and rapid interfacial reaction [50]. The square root of scan rate vs the peak current from AC//MXene (**Figures 8(d)**) shows R^2 values for Ipa and Ipc are 0.31 and 0.99, respectively. Therefore, the CV of AC//MXene exhibits an irreversible reaction as evidenced by broad divergence and significantly shifted peaks observed at various scan rates. Meanwhile, the square root of scan rate vs the peak current from AC//MXene TiO_2 350 °C (**Figure 8(e)**) shows R^2 values for Ipa and Ipc are 0.94 and 0.99. This indicates that the redox reaction that occurs inside the supercapattery is reversible. The CV curves at the various scan rates also show the retained shape with the increment of the scan rates, thus indicating the good reversibility and capability. The oxidation peak is primarily caused by the redox reaction of MXene functional groups (-OH, -F, -O), while the reduction peak is related to the redox activity of TiO_2 [51]. This statement is linear to the appearance of the reduction peak at AC//MXene TiO_2 350 °C at the various scan rates.

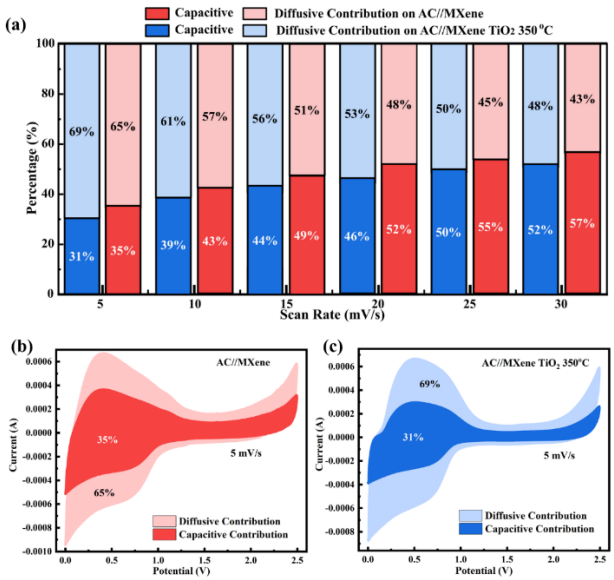

Figure 9 (a) Capacitive and diffusive contribution, and (b-c) CV curve with capacitive and diffusive distribution at the scan rate of 5 mV/s of AC//MXene and AC//MXene TiO_2 350 °C.

Figure 8(f) shows the constant *b* to obtain the dominant storage reaction mechanism of supercapattery. AC//MXene and AC//MXene TiO_2 350 °C exhibit b 0.78 and 0.73, respectively. The b values of supercapattery are higher than the b values of electrodes estimated before by the CV 3-electrode system. The detailed contribution of the diffusion-controlled process and the capacitive-controlled process can be evaluated by obtaining the k_1 and k_2 values from Eq. (8). AC//MXene has k_1 and k_2 values of 6.71×10^{-5} and 2.76×10^{-4}, respectively, while AC//MXene TiO_2 350 °C has k_1 and k_2 values of 6.58×10^{-5} and 3.26×10^{-4}, respectively. Furthermore, **Figure 9(a)** shows the percentage of capacitive and diffusive contributions as a function of the scan rates. At the highest scan rate of 30 mV/s, MXene and MXene TiO_2 350 °C show that 43% and 48% of their capacitance was driven by the diffusion-controlled process. As the scan rates increase, the diffusion-controlled process contribution also increases. At the lowest scan rate of 5 mV/s, MXene and MXene TiO_2 350 °C show that 65% and 69% of their capacitance was driven by the diffusion-controlled process, shown in **Figures 9(b)** and **9(c)**. Thus, increasing the capacitive-controlled contribution of supercapattery was due to the EDLC storage mechanism performed by AC.

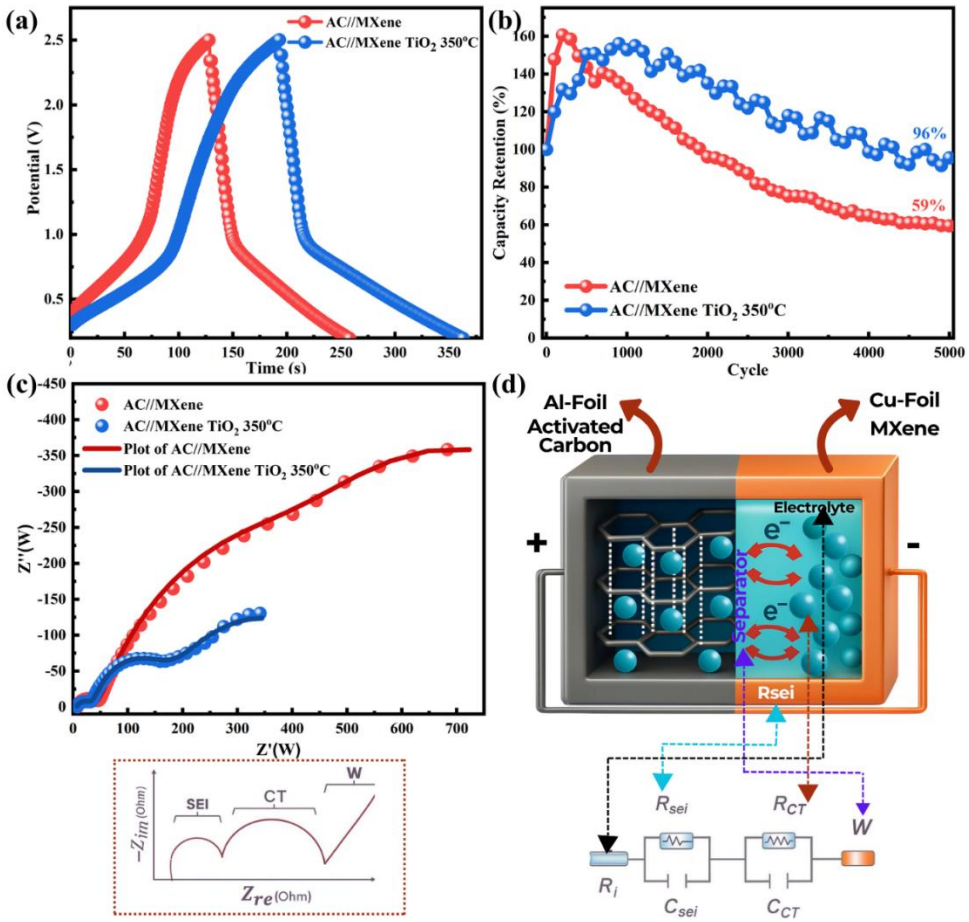

Figure 10 (a) GCD curves at a current density of 0.16 A/g, (b) Capacity retention at a current density of 1.6 A/g, and (c) Nyquist plot of supercapattery based AC//MXene and AC//MXene TiO_2 350 °C.

The GCD test was performed on a supercapattery coin cell device at the potential window of 0 - 2.5 V, same as the CV test. At the current density of 0.16 A/g (**Figure 10(a)**), both AC//MXene and AC//MXene TiO_2 350 °C performed a non-symmetric curve as a signature of the faradaic contribution on the energy storage mechanism [51]. MXene//AC exhibits specific capacitance of 38.51 F/g, energy density of 24.58 Wh/kg, and power density of 686.02 W/kg. After the annealing treatment at a temperature of 350 °C, AC//MXene TiO_2 350 °C shows higher electrochemical performance, including specific capacitance of 49.42

F/g, energy density of 32.88 Wh/kg, and power density of 700.38 W/kg. GCD curves of AC//MXene TiO_2 350 also perform a smaller IR drop (0.12 V) compared to AC//MXene (0.16 V). Furthermore, to analyze the cyclic stability, the supercapattery device was tested at a current density of 1.6 A/g, shown in **Figure 10(b)**. After 5,000 cycles, the AC//MXene TiO_2 350 °C supercapattery retains 96% of the initial capacity, higher than the AC//MXene supercapattery (59%). This result shows that TiO_2 addition can improve the MXene stability [15]. Both supercapattery devices show the gradual increment up to 170% at the 18th cycle for the AC//MXene supercapattery and 159% at the 862nd cycle for the AC//MXene TiO_2 350 °C supercapattery. This is due to the electrode material activation caused by the diffusion of electrolytes into the electrode materials [51]. The surface functional groups have been modified during the cycling process, which facilitates the increasing capacity. Some research shows that the ion intercalation, modification, and reaction among the functional groups can increase the electronic conductivity and charge transport efficiency, leading to an increase in specific capacitance during the cycling process [52]. Supercapattery-based AC//MXene TiO_2 350 °C from this investigation can be compared with the previous research, which is listed in **Table 6**. These results demonstrate that AC//MXene TiO_2 350 °C supercapattery exhibits a practical approach to improving the energy density without sacrificing power density or capacity retention of the device.

Table 6 Supercapattery performance-based AC and MXene comparison to the previous research.

Sample	Electrolyte	Potential window (V)	Cs (F/g)	ED (Wh/kg)	PD (W/kg)	Capacity Retention	Ref
AC//MXene/HKUST	PVA/LiOH	0 - 0.6	31.67	4.0	348	65% after 10,000 cycles at A/g	[51]
GAC//MXene/NiS	2M KOH	0 - 2	56.73	17.69	750	97.7% after 3,000 cycles at A/g	[53]
AC//MXene TiO_2 350 °C	1M Et_4NBF_4	0 - 2.5	49.42	32.88	700.38	96% after 5,000 cycles at 1.6 A/g	This work

The impedance analysis was carried out from the Nyquist plot (**Figure 10(c)**) with the possible circuit model shown in **Figure 10(d)**. This model shares similar characteristics with those found in battery components. Equivalent series resistance (ESR) was obtained from the intercept of the Z'-axis, which relates to the resistance of the current collector/electrode interface, electrolyte ions, and electrode materials [51]. The ESR value of AC//MXene TiO_2 350 °C is 6.13 Ω, lower than that of AC//MXene (8.36 Ω). The first semicircle at the high frequency appeared due to the ion diffusion through the SEI layer during the formation and decomposition of the electrolyte. This region, represented by R and CPE elements, represents the resistance and capacitance of SEI [54]. The first semicircle of AC//MXene TiO_2 350 °C is much lower R_{sei} = 22.62 Ω than AC//MXene R_{sei} = 31.67 Ω. The second semicircle at the middle frequency represents the charge transfer during the electrode reaction, as indicated by the R and CPE elements. The ions adsorb at the surface of the electrode to form a double layer on the interface, and the energy storage process occurs [54]. The second semicircle of AC//MXene TiO_2 350 is also lower, R_{ct} = 87.05 Ω, than AC//MXene R_{ct} = 339.29 Ω. At high frequency, a straight line at an angle close to 45° related to the Warburg impedance represents ion diffusion or transport in the electrolyte and the electrode surface [55]. The slope of AC//MXene TiO_2 350 °C is much higher than that of AC//MXene, indicating the low ion diffusion resistance from the electrolyte to the electrodes [53].

Conclusions

This study successfully demonstrated a controlled thermal oxidation strategy of MXene TiO_2 as a scalable and effective route for fabricating superior electrochemical kinetics and stability of asymmetric supercapattery based on TiO_2 MXene. Crucially, the research identified a key thermal threshold: excessive oxidation at high temperatures led to massive TiO_2

overgrowth, which decreased the SSA by blocking the MXene pores and interlayer spacing (e.g., SSA decreased to 10.3 m^2g^{-1}), even though TiO_2 formation is beneficial. The MXene TiO_2 350 °C sample emerged as the optimal material, striking a precise balance between sufficient TiO_2 growth, successful surface functional group modification by replacing unstable −F groups with oxide groups (Ti-O and Ti-O-Ti bonds) for redox activity, and adequate SSA preservation (25.6 m^2g^{-1}), while maintaining its interlayer spacing (1.89 Å). These characteristics leading kinetic optimization confirmed by CV analysis, which revealed a battery-type behavior dominated by the diffusion-controlled charge storage (up to 93% contribution) rather than surface-limited capacitance. This electrode exhibited a superior specific capacitance of 289.58 F/g at 20 mV/s. Subsequently, the AC//MXene TiO_2 350 °C asymmetric supercapattery device revealed outstanding performance, providing excellent stability (~92% capacity retention after 5,000 cycles) and high metrics (Cs = 49.42 F/g, ED = 32.88 Wh/kg, PD = 700.38 W/kg). Compared to AC//MXene, AC//MXene TiO_2 350 °C showed enhanced kinetics, significantly reduced resistance parameters (ESR, Rsei, Rct), and lower ion diffusion resistance. These findings emphasize the significance of precise oxidation control in tailoring MXene TiO_2 350 °C composites and their surface chemistry, leading to enhanced faradaic kinetics and overall device performance. In summary, this study offers a novel, scalable, and single-step strategy for creating MXene composites for next-generation energy storage applications.

Acknowledgements

This research was funded by the internal competitive Matching Fund grant from the PNBP UM 2024 under contract No. 4.4.624/UN32.14.1/LT/2024.

Declaration of generative AI in scientific writing

For the preparation of this manuscript, especially for the language editing and grammar correction, the authors acknowledge the use of generative AI tools (e.g., QuillBot and ChatGPT by OpenAI). These tools were not used for content generation or data interpretation. The authors take full responsibility for the content and conclusions presented in this work.

CRediT author statement

Nida Usholihah: Conceptualization, Methodology, Writing - Original draft preparation; **Ishmah Luthfiyah**: Data curation, Visualization, Investigation, Writing - Reviewing; **Worawat Meevasana**: Supervision, Investigation, **Herlin Pujiarti**: Supervision, Writing - Reviewing; **Aripriharta**: Software, Validation; **Malik Maaza**: Conceptualization, Methodology; **Muhammad Subhan**: Methodology; **Markus Diantoro**: Supervisio, Writing - Reviewing and Editing.

References

[1] S Jayakumar, PC Santhosh, MM Mohideen and AV Radhamani. A comprehensive review of metal oxides (RuO_2, Co_3O_4, MnO_2 and NiO) for supercapacitor applications and global market trends. *Journal of Alloys and Compounds* 2023; **976**, 173170.

[2] A Sreedhar, MR Pallavolu and JS Noh. Progress in surface and interlayer distance modulated 2D $Ti3C_2$ MXenes for potential flexible supercapacitors: A review. *Applied Materials Today* 2023; **35**, 101942.

[3] D Meena, R Kumar, S Gupta, O Khan, D Gupta and M Singh. Energy storage in the 21st century: A comprehensive review on factors enhancing the next-generation supercapacitor mechanisms. *Journal of Energy Storage* 2023; **72**, 109323.

[4] Q Guo, P Fan, Y Zhang, L Guan, H Wang, A Croft and GZ Chen. Alkali and alkaline earth metals in liquid salts for supercapatteries. *RSC Sustainability* 2024; **2**, 101-124

[5] MI Rosli, FS Omar, R Awang and NM Saidi. Optimization of heating temperature on the growth of manganese sulfide nanosheets binder-free electrode for supercapattery. *Ionics* 2024; **30(1)**, 407-420.

[6] K Karuppasamy, D Vikraman, R Bose, S Hussain, P Santhoshkumar, R Manikandan, J Jung, S Alameri, A Alfantazi and HS Kim. Unveiling the redox electrochemical kinetics of interconnected wrinkled microspheres of binary Cu_2-xSe/Ni1-xSe as battery-type electrode for advanced supercapatteries. *Journal of Colloid and Interface Science* 2024; **654(B)**, 1098-1110.

[7] Y Zhou, L Yin, S Xiang, S Yu, HM Johnson, S

Wang, J Yin, J Zhao, Y Luo and PK Chu. Unleashing the potential of mxene-based flexible materials for high-performance energy storage devices. *Advanced Science* 2024; **11(3)**, 2304874.

[8] Y Guo, Z Du, Z Cao, B Li and S Yang. MXene derivatives for energy storage and conversions. *Small Methods* 2023; **7(8)**, 2201559.

[9] S Panda, K Deshmukh, SKK Pasha, J Theerthagiri, S Manickam and MY Choi. MXene based emerging materials for supercapacitor applications: Recent advances, challenges, and future perspectives. *Coordination Chemistry Reviews* 2022; **462**, 214518.

[10] S Delgado, Y Remedios-Díaz, JC Calderón, S Díaz-Coello, MC Arévalo, G García and E Pastor. Catalytic activity of 2D MXenes toward electroreduction processes: Oxygen reduction and hydrogen evolution reactions. *International Journal of Hydrogen Energy* 2024; **55**, 1050-1061.

[11] P Das, TK Mondal, S Bera, S Das, HL Hsu, YK Su and SK Saha. Facile in-situ growth of spore-like silica on layered MXene sheets for potential application in Supercapacitor. *Electrochimica Acta* 2023; **465**, 142983.

[12] WS Poh, WJ Yiang, WJ Ong, PL Show and CY Foo. Enhancing MXene-based supercapacitors: Role of synthesis and 3D architectures. *Journal of Energy Chemistry* 2024; **91**, 1-26.

[13] S Park, SH Choi, JM Kim, S Ji, S Kang, S Yim, S Myung, SK Kim, SS Lee and KS An. Nanoarchitectonics of MXene derived TiO_2/graphene with vertical alignment for achieving the enhanced supercapacitor performance. *Small* 2023; **20(6)**, 2305311.

[14] AB Tambe, SS Arbuj, GG Umarji, NS Jawale, SB Rane, SK Kulkarni and BB Kale. 2D layered MXene/TiO_2 nano-heterostructures for photocatalytic H2 generation. *Graphene and 2D Materials* 2022; **7(3)**, 91-106.

[15] K Xie, J Wang, K Xu, Z Wei, M Zhang and J Zhang. *In-situ* synthesis of fluorine-free MXene/TiO_2 composite for high-performance supercapacitor. *Arabian Journal of Chemistry* 2024; **17(2)**, 105551.

[16] T Jiang, Y Wang and GZ Chen. Electrochemistry of titanium carbide MXenes in supercapacitor. *Small Methods* 2023; **7(8)**, 2201724.

[17] G Sahu, A Balhara, L Besra, D Nechiyil, K Sudarshan, J Prakash, SK Gupta and S Chatterjee. Defect enriched luminescent MXene-derived TiO for supercapacitors. *Inorganic Chemistry Communications* 2024; **170**, 113462.

[18] W Chen, J Tang, P Cheng, Y Ai, Y Xu and N Ye. 3D porous MXene ($Ti_3C_2T_x$) prepared by alkaline-induced flocculation for supercapacitor electrodes. *Materials* 2022; **15(3)**, 925.

[19] S Kumar, S Aftab, T Singh, M Kumar, S Kumar and Y Seo. Charge storage improvement in uniformly grown TiO_2 on $Ti_3C_2T_x$ MXene surface. *Journal of Alloys and Compounds* 2023; **968**, 172181.

[20] J Hong, C Paeng, S Park, I In, H Lee, NB Velhal, TH Yun, C Jo and C Yim. Flashlight treatment for instantaneous structuring of dense MXene film into porous MXene/TiO_2 nanocomposite for lithium-ion battery anodes. *Chemical Engineering Journal* 2024; **484**, 149598.

[21] EP Simonenko, IA Nagornov, AS Mokrushin, SV Kashevsky, YM Gorban, TL Simonenko, NP Simonenko and NT Kuznetsov. Low temperature chemoresistive oxygen sensors based on titanium-containing Ti_2CT_x and $Ti_3C_2T_x$ MXenes. *Materials* 2023; **16(13)**, 4506.

[22] AA Shamsabadi, H Fang, D Zhang, A Thakur, CY Chen, A Zhang, H Wang, B Anasori, M Soroush, Y Gogotsi and Z Fakhraai The evolution of MXenes conductivity and optical properties upon heating in air. *Small Methods* 2023; **7(10)**, 2300568.

[23] Y Xu, W Lu, G Xu and TW Chou. Structural supercapacitor composites: A review. *Composites Science and Technology* 2021; **204**, 108636.

[24] S Banerjee, B De, P Sinha, J Cherusseri and KK Kar. *Applications of supercapacitors. In*: K Kar (Ed.). Handbook of nanocomposite supercapacitor materials I: Characteristics. Springer, Cham, Switzerland, 2020.

[25] X Zhao, Z Wang, J Dong, T Huang, Q Zhang and L Zhang. Annealing modification of MXene films with mechanically strong structures and high electrochemical performance for supercapacitor applications. *Journal of Power Sources* 2020; **470**, 228356.

[26] NM Keppetipola, M Dissanayake, P Dissanayake,

B Karunarathneb, MA Dourges, D Talagaa, L Servanta, C Olivier, T Toupance, S Uchida, K Tennakonebd, GRA Kumara and L Cojocaru. Graphite-type activated carbon from coconut shell:A natural source for eco-friendly non-volatile storage devices. *RSC Advances* 2021; **11**, 2854-2865

[27] BJ Choudhury, HH Muigai, P Kalita and VS Moholkar. Biomass blend derived porous carbon for aqueous supercapacitors with commercial-level mass loadings and enhanced energy density in redox-active electrolyte. *Applied Surface Science* 2022; **601**, 154202.

[28] S Park, SH Choi, JM Kim, S Ji, S Kang, S Yim, S Myung, SK Kim, SS Lee and KS An. Nanoarchitectonics of MXene derived TiO_2/graphene with vertical alignment for achieving the enhanced supercapacitor performance. *Small* 2024; **20(6)**, 2305311.

[29] A Raza, A Farid, A Rasheed, M Yousaf, IA Khan, KMH Mohammed and MA Ghanem. Home-made chemical vapor deposition-based synthesis of binder-free nanostructured magnesium-molybdenum-sulfide electrode materials for supercapacitor application. *Journal of Physics and Chemistry of Solids* 2024; **192**, 112093.

[30] S Tuntithavornwat, C Saisawang, T Ratvijitvech, A Watthanaphanit, M Hunsom and AM Kannan. Recent development of black TiO_2 nanoparticles for photocatalytic H2 production: An extensive review. *International Journal of Hydrogen Energy* 2024; **55**, 1559-1593.

[31] X Zhang, J Miao, P Zhang, Q Zhu, M Jiang and B Xu. 3D crumbled MXene for high-performance supercapacitors. *Chinese Chemical Letters* 2020; **31(9)**, 2305-2308.

[32] RA Soomro, P Zhang, B Fan, Y Wei and B Xu. Progression in the oxidation stability of MXenes. *Nano-Micro Letters* 2023; **15(1)**, 108.

[33] T Parker, D Zhang, D Bugallo, K Shevchuk, M Downes, G Valurouthu, A Inman, B Chacon, T Zhang, AJ Drexel, CE Shuck, YJ Hu and Y Gogotsi. Fourier-transform infrared spectral library of MXenes. *Chemistry of Materials* 2024; **36(17)**, 8437-8446.

[34] M Hou, B Miao, M Asad, Y Zhang, Q Chen, M Zhang, Z Bai, Y Zhao and G Liu. Efficient photocatalytic degradation of aqueous organic pollutants by using an advanced TiO_2/Ti_3C_2/montmorillonite composites. *Journal of Alloys and Compounds* 2024; **976**, 173362.

[35] P Karthikeyan, K Ramkumar, K Pandi, A Fayyaz, S Meenakshi and CM Park. Effective removal of Cr(VI) and methyl orange from the aqueous environment using 2-dimensional (2D) $Ti_3C_2T_x$ MXene nanosheets. *Ceramics International* 2021; **47(3)**, 3692-3698.

[36] M AhadiParsa, A Dehghani and B Ramezanzadeh. Titanium carbide-based (Ti_3C_2) MXene@Zn-doped-S-polyaniline nanosheets: Toward thermo-mechanical and UV-shielding properties enhancement. *Journal of the Taiwan Institute of Chemical Engineers* 2024; **156**, 105364.

[37] K Gothandapani, GT Selvi, RS Jennifer, V Velmurugan, S Pandiaraj, M Muthuramamoorthy, S Pitchaimuthu, V Raghavan, ACJ Malathi, A Alodhayb and AN Grace. Ni-Ti_3C_2 MXene composite derived from Ni-metal organic framework for electrochemical hydrogen evolution reaction in acidic and alkaline medium. *International Journal of Hydrogen Energy* 2024; **52(D)**, 1164-1171.

[38] T Cygan, J Wozniak, M Petrus, A Lachowski, W Pawlak, B Adamczyk-Cieślak, B Adamczyk-Cieślak, A Jastrzębska, A Rozmysłowska-Wojciechowska, T Wojciechowski, W Ziemkowska and A Olszyna. Microstructure and mechanical properties of alumina composites with addition of structurally modified 2d Ti_3C_2 (Mxene) phase. *Materials* 2021; **14(4)**, 829.

[39] H Xue, Q Yan, L Chen, Y Wang, X Xie and J Sun. Ti_3C_2 MXene assembled with TiO_2 for efficient photocatalytic mineralization of gaseous o-xylene. *Applied Surface Science* 2023; **608**, 155136.

[40] R Bardestani, GS Patience and S Kaliaguine. Experimental methods in chemical engineering: Specific surface area and pore size distribution measurements - BET, BJH, and DFT. *The Canadian Journal of Chemical Engineering* 2019; **97(11)**, 2781-2791.

[41] J Yu, M Zeng, J Zhou, H Chen, G Cong, H Liu, M Ji, C Zhu and J Xu. A one-pot synthesis of nitrogen doped porous MXene/TiO2 heterogeneous film for high-performance flexible energy storage.

Chemical Engineering Journal 2021; **426**, 130765.

[42] S Ghotia, A Kumar, V Sudarsan, N Dwivedi, S Singh and P Kumar. Multilayered $Ti_3C_2T_x$ MXenes: A prominent materials for hydrogen storage. *International Journal of Hydrogen Energy* 2024; **52**, 100-107.

[43] A Numan, S Rafique, M Khalid, HA Zaharin, A Radwan, NA Mokri, OP Ching and R Walvekar. Microwave-assisted rapid MAX phase etching and delamination: A paradigm shift in MXene synthesis. *Materials Chemistry and Physics* 2022; **288**, 126429.

[44] JB Lee, GH Choi and PJ Yoo. Oxidized-co-crumpled multiscale porous architectures of MXene for high performance supercapacitors. *Journal of Alloys and Compounds* 2021; **887**, 161304.

[45] M Cao, F Wang, L Wang, W Wu, W Lv and J Zhu. Room temperature oxidation of Ti_3C_2 MXene for supercapacitor electrodes. *Journal of The Electrochemical Society* 2017; **164(14)**, A3933.

[46] H Hassan, U Romman, MW Iqbal, AM Afzal, T Yaseen, MA Sunny, S Mohammad, NH Alotaibi and M Manzoor. Synergistic hybridization of Mn-MOF@rGO and Ti_3C_2 for high-performance supercapattery devices and hydrogen evolution reaction. *Materials Chemistry and Physics* 2024; **327**, 129914.

[47] G Sriram, G Hegde, K Dhanabalan, Y Kalegowda, D Mouraliraman, RS Vishwanath, M Kurkuri and TH Oh. Recent trends in hierarchical electrode materials in supercapacitor: Synthesis, electrochemical measurements, performance and their charge-storage mechanism. *Journal of Energy Storage* 2024; **94**, 11254.

[48] RRB Rakhi, B Ahmed, MN Hedhili, DH Anjum and HN Alshareef. Effect of Postetch annealing gas composition on the structural and electrochemical properties of Ti_2CT_x MXene electrodes for supercapacitor applications. *Chemistry of Materials* 2015; **27(15)**, 5314-5323.

[49] Q Wang, Z Zhang, L Wang, Y Zhang, X Zhou and G Ma. Ultrafast fabrication of TiO_2-inlaid multilayered carbon for supercapacitor. *ChemistrySelect* 2018; **3(38)**, 10811-10814.

[50] M Ahmed, N Ahmed, H Ahmad, S Bashir, R Subramaniam and G Ali. A comparative study on exploring sputtered titanium nitride thin films for high-performance supercapacitors. *Journal of Energy Storage* 2025; **105**, 114712.

[51] R Ismail, NHN Azman, D Mohanadas, MN Mustafa, MAAM Abdah, V Raman, J Abdullah and Y Sulaiman. Facile ultrasonication synthesis of MXene/HKUST-1 composite as positive electrode for supercapattery. *Journal of Energy Storage* 2024; **94**, 112461.

[52] AH Rumman, S Mahmud, NT Mim, J Akter, A Roy, AR Nirjhar, NA Dipon, S Islam, A Gafur, AN Ahmed and K Shorowordi. Cold sintered TiO_2-$Ti_3C_2T_x$ MXene electrode materials. *Materials Advances* 2025; **6(18)**, 6454-6468.

[53] H Liu, R Hu, J Qi, Y Sui, Y He, Q Meng, F Wei, Y Ren and Y Zhao. A facile method for synthesizing NiS nanoflower grown on MXene ($Ti_3C_2T_x$) as positive electrodes for 'supercapattery'. *Electrochimica Acta* 2020; **353**, 136526.

[54] LA Santa-Cruz, FC Tavares, LF Loguercio, CIL Dos Santos, RA Galvão, OAL Alves, MZ Oliveira, RM Torresi and G Machado. Electrochemical impedance spectroscopy: From breakthroughs to functional utility in supercapacitors and batteries - a comprehensive assessment. *Physical Chemistry Chemical Physics* 2024; **26**, 25748-25761

[55] M Rizan, V Samaje, K Kumara, KN Ravindra and S Thiyagaraj. Hydrothermal synthesis of Bi_2S_3 nanoparticle as a prospective electrode for supercapacitor. *Next Materials* 2024; **2**, 100081.